RSC Advances

PAPER

View Article Online
View Journal | View Issue

Open Access Article. Published on 20 March 2017. Downloaded on 7/19/2025 8:50:37 AM.
This article is licensed under a Creative Commons Attribution-NonCommercial 3.0 Unported Licence.

Cite this: *RSC Adv.*, 2017, **7**, 17368

Theoretical investigation on the effect of ancillary ligand modification for highly efficient phosphorescent platinum(II) complex design†

Hong-Wei Fan, Fu-Quan Bai,* Zhi-Xiang Zhang, Yu Wang, Ze-Xing Qu, Rong-Lin Zhong and Hong-Xing Zhang*

In this study, density functional theory (DFT) and time-dependent density functional theory (TDDFT) calculations were employed to investigate the geometries, electronic structures, reorganization energy (λ) and photophysical properties of four cyclometalated Pt(II) complexes (bzq)Pt(dpm) (**1**), (bzq)Pt(ppy) (**2**), (bzq)Pt(Ncaz) (**3**) and (bzq)Pt(Ndbt) (**4**) (where bzq = benzo[*h*]quinoline, dpm = dipivolylmethanoate, ppy = 2-phenylpyridine, Ncaz = *N*-substituted carbazole and Ndbt = *N*-substituted dibenzothiophene). In addition, the radiative decay processes and zero-field splitting were calculated based on the spin–orbit coupling (SOC) effect, and nonradiative decay pathways were discussed to evaluate the phosphorescence efficiency qualitatively. All the complexes retain the bzq as a cyclometalated ligand and our research focuses on the role recognition of another ancillary ligand modification theoretically. According to the results, in complexes **2–4** replacing the dpm with different ligands shows better rigidity which may weaken the nonradiative decay pathways and enhance the capability of charge transfer. Furthermore, complexes **1–4** tend to be bluish-green luminescent materials, and the emission wavelengths of **1**, **2** and **4** are close to each other due to the similar excited state energy levels and electronic density distribution. Compared with complex **1**, the radiative decay rate constants (k_r) of **2–4** are greatly increased. Therefore, the designed complexes would be potential phosphorescence materials because of their high phosphorescence quantum efficiency and complex **3** can also serve as a promising bipolar transporting material due to its better charge transfer balance character.

Received 17th January 2017
Accepted 8th March 2017

DOI: 10.1039/c7ra00705a

rsc.li/rsc-advances

1 Introduction

Over the past decades, organic light emitting diodes (OLEDs) have obtained a great deal of attention due to their flexibility in flat-panel displays.[1,2] They are widely used in digital products and solid-state lighting devices.[3–6] Phosphorescent transition-metal compounds have excellent performances as triplet dopant emitters in OLED emission layers, especially those of Ir(iii) and Pt(II) complexes. They are heavy metal atoms that can induce strong spin–orbit coupling (SOC) and promote an effective intersystem crossing (ISC), which results in higher quantum efficiency.[7–11] Platinum which has the second largest SOC constant, tends to form planar structure due to the d^8-electron configuration of the Pt(II) ion. The ligand of cyclometalated Pt(II) complexes can be designed as bidentate, tridentate and tetradentate. The diversity of these ligands can greatly affect the phosphorescence properties.[12–16] As we know, the singlet excited states convert to the triplet states through ISC due to the SOC and then the triplet excited states return to the ground state, phosphorescence can be achieved through the radiative decay process. Nevertheless, if nonradiative decay holds a large proportion in the whole decay process, there will be weak or no phosphorescence.[17] Therefore, the key to improve the efficiency of electroluminescent emitters are to increase the radiative decay rate constants and decrease the nonradiative decay rate constants.[18]

Generally, chelating ligands of transition-metal complexes, which play a critical role in the OLEDs, include the cyclometalated ligands and ancillary ligands. The cyclometalated ligands have influence on the charge transition between metal and ligand (MLCT) at the excited states, and then alter the emission wavelengths.[19] Moreover, ancillary ligands provide the ligand fields and affect the relative energy of metal center, such as β-diketonate and picolinate.[20,21] Previous researches have demonstrated that the phosphorescence properties would be easily tuned mostly by the variation of cyclometalated ligands, while the change of ancillary ligands has little influence.[22,23] Recently, ancillary ligands can affect the phosphorescence

International Joint Research Laboratory of Nano-Micro Architecture Chemistry, Laboratory of Theoretical and Computational Chemistry, Institute of Theoretical Chemistry, Jilin University, Changchun 130023, China. E-mail: baifq@jlu.edu.cn; zhanghx@mail.jlu.edu.cn

† Electronic supplementary information (ESI) available: Details of calculated molecular orbital (MO) compositions, NTOs, the coupling energy levels and transition characters analysis between singlet excited states and triplet excited states for complexes **1–4**. See DOI: 10.1039/c7ra00705a

This journal is © The Royal Society of Chemistry 2017

Open Access Article. Published on 20 March 2017. Downloaded on 7/19/2025 8:50:37 AM.
This article is licensed under a Creative Commons Attribution-NonCommercial 3.0 Unported Licence.

efficiency evidently through altering the properties of excited-state was recorded.[24] Thus, the modification of ancillary ligands becomes the focus for the highly efficient of transition-metal complexes.[25,26] In this respect, the heteroleptic C^N ligands such as phenyl-pyrazole (ppy) and phenyl-pyrazole (ppz) were widely applied in transition metal complexes.[27–30] The C^N ligand can bind to metals forming a five-membered chelate through the N atom of pyridine ring and C atom of phenyl. The anionic C atom related to the metal centre is a strong σ-donor while the pyridyl ring maintains a favourable π-acceptor. The C^N ligands provide the metal ion a strong ligand field which leads to a higher energy of deactivating d–d states and reduces the thermal quenching compared to homologous N^N ligands.[31,32] Lately, the carbazole group has been used to improve the rigidity and performance of complexes. As reported by Hang and co-workers, a series of highly efficient cyclometalated Pt(II) complexes were synthesized and the maximum external quantum efficiency value as high as 23.7% were achieved by introducing a carbazole group in ligand.[33] Based on this knowledge, the N atom on the carbazole group is substituted by the S atom to foresee new structure. Recent research in Thompson group, they have synthesized and reported a series of novel bidentate Pt(II) complexes.[34] Among these complexes, the suitable complex **1** has still the small value of nonradiative decay rate constant. Based on the complex **1**, complexes **2–4** in Fig. 1 are tried to be designed by replacing the dpm ligand with different ancillary ligands mentioned above to seek the better candidates. Herein, as the highly efficient phosphorescent OLED materials, the newly designed complexes are expected to improve the radiative decay rate constant and strengthen the stability.

In order to gain a deep insight into the effects of ancillary ligands on the photophysical properties and quantum efficiency of these complexes, DFT and TDDFT methods have been adopted to investigate the electronic structures, charge transport abilities and emission properties of the complexes **1–4**. The radiative decay rate (k_r) and zero-filed splitting values are quantitatively evaluated by the calculation of SOC matrix elements; nonradiative decay rate (k_{nr}) is qualitatively discussed *via* energy gap law and the relative energy between metal-centered (^{3}MC) state and minimum energy crossing point (MECP).[17,35,36] Reorganization energy (λ) is an important factor in evaluating the balance between the electron and hole transport of the luminescent materials. The theoretical calculation results reveal that complexes **2** and **4** would be better phosphorescent materials for the high phosphorescence quantum efficiency and complex **3** can serve as promising bipolar candidate due to the balanced charge carrier injection and transport feature. We hope that our preliminary study could provide useful information for the further design and application of highly efficient luminescent material in OLEDs.

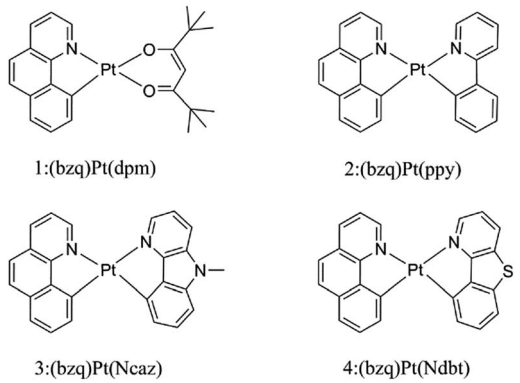

Fig. 1 Chemical structures of the investigated complexes **1–4**.

2 Theory of computation

2.1 Theoretical background

Generally speaking, the phosphorescence quantum efficiency of transition metals is decided by radiative decay and nonradiative decay rates. According to the energy gap law, the nonradiative decay rate constant (k_{nr}) from T_m to S_0 states can be evaluated by the equation:[37,38]

$$k_{nr}(T_m \rightarrow S_0) \propto \exp\{-\beta[E(T_m) - E(S_0)]\} \quad (1)$$

The parameter β is involved with the structural distortion between the ground and correlative excited triplet states. $[E(T_m) - E(S_0)]$ is the energy gap between excited state and ground state. Hence, the smaller structural distortion and larger energy gap between excited triplet and ground state would be beneficial to decrease the nonradiative decay rate.

On the basis of Born–Oppenheimer approximation and the first order perturbation theory, the phosphorescent radiative decay rate constant (k_r) that from T_m to S_0 can be expressed as follows:[39,40]

$$k_r^{\alpha}(T_m \rightarrow S_0) = \frac{16 \times 10^6 \pi^3 E(T_m)^3 \eta^3}{3h\varepsilon_0} \left\{ \sum_n \frac{\langle T_m^{\alpha} | H_{SOC} | S_n \rangle}{E(S_n) - E(T_m)} M_{S_n} \right\}^2 \quad (2)$$

where η means the refractive index of the cyclohexane solution which is taken to be 1.43. $E(S_n)$ represents the vertical excitation energy from the nth singlet excited (S_n) to ground state (S_0) transition. $E(T_m)$ represents the vertical excitation energy from the mth triplet excited state (T_m) to S_0 transition. $\langle T_m^{\alpha} | H_{SOC} | S_n \rangle$ is the SOC matrix element ($\alpha = x, y$ or z). M_{S_n} is the transition dipole moment from S_0 to S_n, which can be defined by the following equation:

$$M_{S_n} = \left(\frac{3he^2}{8\pi^2 m_e c} \times \frac{f_n}{E(S_n)} \right)^{\frac{1}{2}} \quad (3)$$

It is obvious that the M_{S_n} is connected with the oscillator strength (f_n) and transition energy ($E(S_n)$). Where e is the electron charge; m_e and c are the mass of an electron and light speed. Combined with the eqn (2) and (3), the k_r is represented in the form:

$$k_r^{\alpha}(T_m \rightarrow S_0) = \frac{\eta^3}{1.5} E(T_m)^3 \left\{ \sum_n \frac{\langle T_m^{\alpha} | H_{SOC} | S_n \rangle}{E(S_n) - E(T_m)} \left(\frac{f_n}{E(S_n)} \right)^{1/2} \right\}^2 \quad (4)$$

Open Access Article. Published on 20 March 2017. Downloaded on 7/19/2025 8:50:37 AM.
This article is licensed under a Creative Commons Attribution-NonCommercial 3.0 Unported Licence.

Under the Boltzmann statistics distribution, the triplet sublevels are postulated at thermal equilibrium. Thus, the k_r can be calculated as the vectorial summation of k_r^{α} values as follows:[41,42]

$$k_r = \frac{1}{3}\sum_{\alpha} k_r^{\alpha} \tag{5}$$

As we all know, the triplet state splits into three spin triplet sublevels duo to the SOC effect. Zero-field splitting (ZFS) is defined as the energy splitting between the first and third sublevel, which is related to the composition of MLCT in emission excited and the magnitude of k_r values.[43,44] The ΔE(ZFS) can be described in the form:

$$\Delta E(T_m^{\alpha}) = \sum_n \frac{|\langle T_m^{\alpha}|H_{SOC}|S_n\rangle|}{E(S_n) - E(T_m)} \tag{6}$$

where α is the three sublevels of energy shift.

2.2 Computational details

All the calculations were performed by the Gaussian 09 software package with a tight self-consistent convergence threshold to ensure optimization and wave functions convergence.[45] The geometry optimization and phosphorescent properties were evaluated by DFT and TDDFT. In the process of optimization, vibrational frequencies were calculated with no imaginary frequencies, indicating the optimized structures are at the minima of the potential energy surface. Since the experimental data was obtained in cyclohexane solution, the solvent effect by utilizing the Polarizable Continuum Model (PCM) was taken into account in the geometry optimization and phosphorescence properties.[46,47] In addition, Hay and Wadt's[48] quasi-relativistic effective core potential (ECP) with 18 valence electrons as well as the "double-ζ" quality basis set LANL2DZ were adopted for platinum atom and the 6-31G(d) basis set was applied to the non-metallic atoms such as C, H, O, N and S atoms.

It is important to choose a reliable exchange–correlation functional for the current system. Considering the charge-transfer of ligand to metal in transition metal complexes, five widely used exchange–correlation functionals containing the B3LYP,[49] B3P86,[50] PBE0,[51] M062X,[52] and CAM-B3LYP[53] were employed for the singlet ground state of complex **1** compared to its crystal X-ray structure. The corresponding parameters of the optimized ground state geometry together with experimental values are listed in Table 1. The results show that PBE0 can give an accurate geometry structure among these functionals because its average relative error is the smallest. Thus, the optimization of the ground states and the lowest triplet excited states for complexes **1–4** were calculated with PBE0 functional in the studied system.

Owing to spin flipped in triplet states, we also find a responsible method to predict the emission properties, five different functionals were performed on the lowest-lying emission wavelength of triplet state for complex **1**. On one hand, through the calculation of five functionals, the transition properties of lowest triplet excited state (T_1) are similar. On the other hand, the calculated lowest-lying emission wavelengths are 697 nm, 667 nm, 739 nm, 658 nm, 537 nm with PBE0, B3P86, CAM-B3LYP, B3LYP, M06-2X functionals, respectively. From the result, the wavelength calculated by M06-2X functional is in good agreement with the experimental value of 505 nm. Besides, for the assessment of singlet–triplet transition energies based on the TDDFT, M06-2X is regarded as the most accurate functional which can adopt inner track to estimate with the mean absolute error close to 0.25 eV in most cases.[54] In short, the PBE0 functional was used to optimize the singlet ground state and the triplet state geometric structures for all complexes in the current system, while the emission energies were analyzed by M06-2X functional.

3 Results and discussion

3.1 Geometries in ground and lowest-lying triplet excited states

The optimized structures at ground-state along with some atomic labels of the complexes are shown in Fig. 2. It can be seen that these Pt(II) complexes with d^8 configuration present a square geometry. To gain a better understanding of the influence about different ligands, some changes of geometry parameters for all complexes are discussed in both S_0 and T_1 states. The main bond distances and angles between metal center Pt(II) and relevant atoms as well as dihedral angle at S_0 and T_1 states are listed in Table 2.

From the results, the bond lengths of Pt–N1 are about 0.182 Å longer than Pt–C2 in complexes **1–4**, indicating that the coordinated bond between atoms C and Pt is stronger than the

Table 1 Optimized geometric parameters at the singlet ground state of complex **1** by different functionals as well as the experimental values (Å)

Item	Expt[a]	PBE0	Relative error	B3LYP	Relative error	B3P86	Relative error	M062X	Relative error	CAM- B3LYP	Relative error
Pt–N1	1.983	2.013	1.5%	2.039	2.8%	2.016	1.7%	2.039	2.8%	2.030	2.4%
Pt–C2	1.990	1.978	0.6%	1.996	0.3%	1.978	0.6%	1.967	1.2%	1.988	0.1%
Pt–O3	2.029	2.015	0.7%	2.034	0.3%	2.014	0.7%	2.037	0.4%	2.018	0.6%
Pt–O4	2.032	2.110	3.8%	2.137	5.2%	2.113	4.0%	2.157	6.2%	2.115	4.1%
C7–C8	1.428	1.417	0.7%	1.420	0.6%	1.414	1.0%	1.423	0.4%	1.420	0.6%
Average relative error			1.46%	—	1.84%	—	1.60%	—	2.20%	—	1.56%

[a] The experimental data is obtained from ref. 34.

 This journal is © The Royal Society of Chemistry 2017

Open Access Article. Published on 20 March 2017. Downloaded on 7/19/2025 8:50:37 AM.
This article is licensed under a Creative Commons Attribution-NonCommercial 3.0 Unported Licence.

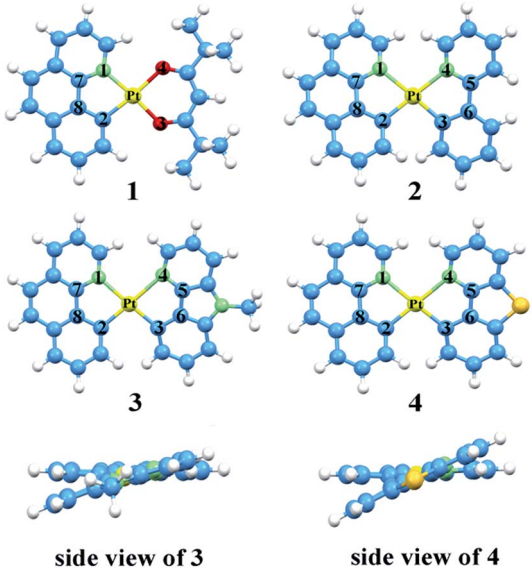

Fig. 2 Vertical view of the optimized geometries for **1**–**4** with the side view for **3** and **4** at the singlet ground state.

Pt–N. Meanwhile, the Pt–N3 and Pt–C4 are also consistent with the above property. At the S_0 state, the Pt–N1 bond lengths of **2**–**4** are elongated by 0.125–0.165 Å compared with complex **1**, which can be attributed to the *trans* effect in different ligands.[55,56] In addition, compared with complexes **3**–**4**, the bond lengths of Pt–C3 and Pt–N4 on the ppy ligand of **2** are shorter, while Pt–N1 and Pt–C2 bond lengths on the bzq ligand are elongated. These values reveal that the introduction of ppy ligand can increase its interaction with the metal atom and decrease the interaction between other ligand and metal atom. Obviously, the bond length of C5–C6 in **3** and **4** are shortened by 0.046–0.057 Å, due to the substitution of ppy in the positions of both beta carbons by N and S atom to form Ncaz and Ndbt, which may strengthen the ligand internal–conjugation interaction. While, for C7–C8, the slight change within 0.008 Å can be ignored. For the relevant bond angles of Pt and two ligands, except for the C2–Pt–N1, the difference of others are induced by the five-member rings between Pt and ancillary ligands.

Since the S_0 and T_1 states participate in the process of phosphorescence, the geometry structures of T_1 state worth noticing. The bond lengths of Pt–N1 and Pt–C2 for all complexes are shorter than the ground state. In other words, the bonds between metal and ligands are strengthened, which is likely to promote the charge transfer transition from metal centre to ligands. While the bond angles from S_0 to T_1 states have no distinct variation, especially for the designated complexes **2**–**4**. The dihedral angle differences between S_0 and T_1 states for all complexes are less than 2.0°. It is turned out that the complexes show better rigidity, which brings about a smaller nonradiative rate (k_{nr}).[35]

3.2 Frontier molecular orbital properties

In order to clearly reveal the electronic excitation of these Pt(II) complexes, it is essential to further investigate the frontier molecular orbital (FMOs), especially the highest occupied molecular orbital (HOMO) and lowest unoccupied molecular orbital (LUMO). The relevant orbital analysis along with the energy gaps at the S_0 state are displayed in Fig. 3. The orbital compositions and distributions of selected FMOs are presented in Tables S2–S5 and Fig. S1.†

For the electron density distributions of the HOMO, complex **1** is mainly located in 5d(Pt) orbitals, the π orbitals of bzq and dpm ligands. Obviously, the electron density distributions of HOMO for complexes **2** and **4** are rather similar, which are resided on the 5d(Pt) orbitals and bzq ligand. Complex **3** is predominantly centralized on the 5d(Pt) orbitals and the π orbitals of Ncaz ligand. It is worth noting that the energy differences between HOMO and HOMO−1 of complexes **1**–**4** are 0.43 (**1**), 0.10 (**2**), 0.14 (**3**) and 0.04 eV (**4**) with the order of **4** < **2** <

Table 2 Selected main geometry parameters for **1**–**4** at the ground and lowest-lying triplet excited states

	1		**2**		**3**		**4**	
Item	S_0	T_1	S_0	T_1	S_0	T_1	S_0	T_1
Bond length (Å)								
Pt–N1	2.013	2.010	2.178	2.169	2.138	2.134	2.150	2.143
Pt–C2	1.978	1.970	1.996	1.989	1.971	1.965	1.981	1.975
Pt–O/C3	2.015	2.019	1.989	1.994	2.021	2.027	2.012	2.018
Pt–O/N4	2.110	2.102	2.153	2.151	2.404	2.395	2.282	2.277
C5–C6	—	—	1.460	1.462	1.403	1.403	1.414	1.415
C7–C8	1.417	1.430	1.425	1.440	1.424	1.439	1.423	1.400
Bond angle [degree]								
C2–Pt–N1	82.16	81.48	79.94	79.48	81.24	80.65	80.77	80.24
N1–Pt–O1/N4	92.86	93.58	103.4	103.3	97.80	98.12	100.4	100.4
N/O4–Pt–O/C3	91.65	91.29	79.51	79.55	82.89	82.89	81.85	81.85
C/O3–Pt–C2	93.33	93.65	100.5	101.0	99.13	99.60	98.90	99.49
Dihedral angle [degree]								
N4–C3–Pt–N1	0.04	−0.01	103.9	103.8	95.96	98.02	103.4	103.6

Open Access Article. Published on 20 March 2017. Downloaded on 7/19/2025 8:50:37 AM.
This article is licensed under a Creative Commons Attribution-NonCommercial 3.0 Unported Licence.

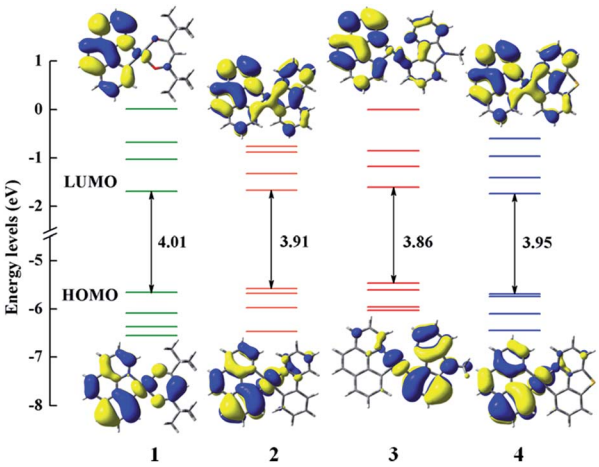

Fig. 3 Frontier molecular orbital energy levels, energy gaps (in eV) and orbital composition distributions of the HOMO and LUMO at the S_0 state for **1–4**.

3 < **1**. It has been confirmed that the H_{SOC} matrix element will be increased when the two highest occupied orbitals get close, which leads to a large radiative decay rate.[14] Obviously, there are obvious differences in LUMO distributions of **2–4** compared with **1**. The LUMO of **2** and **4** are delocalized on all ligands, while that in **1** is mainly centralized on the π* orbitals of bzq and a smaller contribution from 5d orbitals of metal center. Combined with the diagram and data, metal 5d(Pt) orbitals provide much contribution for the HOMO and the ligands constitute the majority of LUMO in all complexes, which demonstrates the transition nature from the HOMO to LUMO are metal-to-ligand transfer (MLCT) mixed with ligand-to-ligand (LLCT). As presented in the Fig. 3, the HOMO–LUMO gaps of complexes **2–4** are smaller owing to introducing the different ligands. So the transition from HOMO to LUMO is effective and the higher HOMO energy leads to a better ability of hole-injection compared with **1**. In addition, the LUMO energy level of **4** is calculated to be −1.743 eV, which is lower than other complexes. The lower LUMO energy level could be caused by the better electron delocalization in the entire molecule to stabilize the unoccupied molecular orbitals. According to the calculated results, different ancillary ligands have significant influence on the distribution of FMOs, which may alter the energy gap and phosphorescence efficiency.

3.3 Charge transportation properties

It is known that low energy barrier for the injection and transport balance between the hole and electron of luminescent complexes are pivotal for the high performance OLEDs. In order to quantitatively discuss the charge injection properties, the ionization potential (IP) and electron affinity (EA) have been calculated by DFT method, which are closely related to the HOMO and LUMO, respectively.[55] In addition, there are vertical (IP_v/EA_v) and adiabatic (IP_a/EA_a) two processes. For photoluminescent materials, a smaller IP value implies easier hole injection ability. On the other hand, a larger EA value facilitates the electrons injection capacity. The hole extraction potential (HEP) and electron extraction potential (EEP) are studied to evaluate the extraction potentials of the hole and electron.

According to the semiclassical Marcus theory,[57] the intermolecular charge (hole and electron) transfer rate (K_{et}) can be expressed as follows:

$$K_{et} = \left(\frac{4\pi^2}{h}\right)\frac{V^2}{\sqrt{4\pi\lambda K_B T}}\exp\left(-\frac{\lambda}{4K_B T}\right) = A\exp\left(-\frac{\lambda}{4K_B T}\right) \quad (7)$$

where T and K_B are the temperature and Boltzmann constant, respectively. λ represents the reorganization energy. h is the Plank constant. V is the electronic coupling terms for the adjacent molecules in the dimensional stacking, which is determined by the overlap of molecular orbitals. As shown in eqn (7), the K_{et} is governed by two major factors that are λ and V, respectively. Herein, taking the crystal structure of experimental complex **1** as example, the V of hole and electron are calculated through employing ADF program package[58] with PBE0/TZP method. From the calculation results, the V of **1** for electron transfer is 0.0510 eV, and for hole transfer is 0.0156 eV, respectively. In comparison with previous work, it is negligibly small.[59] Meanwhile, owing to the restricted intermolecular charge transfer range in solid state, the transfer rate of charge has been indicated to be mainly affected by reorganization energy λ.[60,61] From the eqn (7), a smaller λ is the key factor for the faster charge transport property, which can be defined by the following relations:

$$\lambda_h = \lambda_0 + \lambda_+ = IP_v - HEP \quad (8)$$

$$\lambda_e = \lambda_0 + \lambda_- = EEP - EA_v \quad (9)$$

All the relevant calculation values of complexes **1–4** are shown in Table 3.

As can be seen in Table 3, complexes **2** and **3** have smaller IP values which are related to their higher HOMO energy levels than complex **1**. Namely, the complexes **2** and **3** have better hole injection ability due to the introduction of ppy and Ncaz ligands. Meanwhile, the EA values of complexes **2** and **4** are larger than others, which can enhance electron injection ability and agree with their lower LUMO energy. From the Table 3, the reorganization energies of electron (λ_e) transport of all complexes are smaller than their hole (λ_h) except for **1**. Therefore, the complexes replaced the dpm with different ligands tend to be electron transporting materials. In addition, complex **3** is the promising bipolar transporting material because the difference between hole and electron reorganization values are

Table 3 Ionization potentials (IPs), extraction potentials, electron affinity (EAs) and reorganization energy (λ) of **1–4** (unit in eV)

	IP(v)	IP(a)	HEP	EA(v)	EA(a)	EEP	λ_{hole}	λ_e
1	6.85	6.77	6.68	0.29	0.42	0.56	0.17	0.27
2	6.74	6.57	6.19	0.43	0.52	0.61	0.54	0.18
3	6.62	6.51	6.39	0.32	0.41	0.50	0.23	0.18
4	6.82	6.75	6.44	0.54	0.62	0.71	0.38	0.17

 This journal is © The Royal Society of Chemistry 2017

Open Access Article. Published on 20 March 2017. Downloaded on 7/19/2025 8:50:37 AM.
This article is licensed under a Creative Commons Attribution-NonCommercial 3.0 Unported Licence.

quite small (0.05 eV), which is an important factor for the OLEDs devices. Generally speaking, the ancillary ligands can not only increase the abilities of hole and electron injection but also affect the balance of charge transfer.

3.4 Phosphorescence emission properties

On the basis of the optimized lowest triplet excited-state geometries, the phosphorescence properties of all the investigated complexes were calculated. The results including the lowest energy emission wavelengths and transition characters are shown in Table 4. The natural transition orbitals (NTOs) of complexes **1–4** are plotted in Fig. 4 and S2.† The unoccupied NTOs refer to the as "electron" transition orbitals while the occupied NTOs mean the "hole" transition orbitals. Furthermore, the orbital compositions distribution related to phosphorescence emission of complexes **1–4** are summarized in Table S6.†

As we can know from the Table 4, the calculated emission wavelength is 537 nm for complex **1**, which matches well with the experimental value of 505 nm. The phosphorescence emissions of **2–4** at 535, 529, and 532 nm are slightly hypochromatic shifted (2–8 nm) compared with that of **1**, which reveals that the designed complexes **2–4** have a great trend to be bluish-green luminescent materials. Meanwhile, the emission wavelengths of complexes **1**, **2** and **4** are nearly the same due to the similar electronic density distribution between HOMO and LUMO. Additionally, the T_1 states of these complexes are originated largely from HOMO to LUMO. As shown in Fig. 4 and S2,† for complexes **1–4**, the NTO hole is largely distributed in the metal Pt and bzq ligand, while the NTO electron is delocalized in the bzq ligand. Thus, the transition natures of the investigated complexes at T_1 state are assigned as ^{3}MLCT/^{3}LC$_{bzq}$. In Table S6,† the compositions of 5d(Pt) orbitals have not much differences and be retained for these new complexes, and the LUMO of the studied complexes are all located in bzq ligand, indicating the bzq ligand is the main ligand in this system. For complexes **1**, **2** and **4**, the HOMO orbitals are centred on the 5d(Pt) orbitals and bzq moieties. The transition of H → L is assigned as [d(Pt) + π(bzq) → π*(bzq)] with ^{3}MLCT/^{3}ILCT (inter-ligand charge transfer) transition characters. However, it can be found that the HOMO of complex **3** is localized on 5d(Pt) orbitals, bzq and Ncaz ligands, it is described as [d(Pt) + π(bzq) +π(C^N) → π*(bzq)] with ^{3}MLCT/^{3}LLCT transition characters.

Table 4 Calculated phosphorescent emissions of complexes **1–4** together with the experimental value

	States	λ (nm)/ E (eV)	λ_{expt} (nm)	Main configuration	Assignment
1	T_1	537/2.31	505	H → L (72%)	MLCT/ILCT
				H-2 → L (14%)	MLCT/ILCT
2	T_1	535/2.32		H → L (67%)	MLCT/ILCT
				H → L + 1 (10%)	MLCT/ILCT
3	T_1	529/2.34		H → L (52%)	MLCT/LLCT
				H-1 → L (17%)	MLCT/LLCT
4	T_1	532/2.33		H → L (65%)	MLCT/ILCT
				H → L + 1 (10%)	MLCT/LLCT

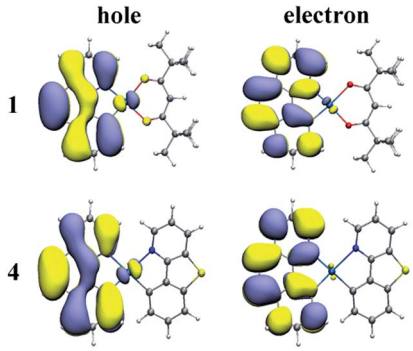

Fig. 4 NTO plots at the optimized T_1 states for **1** and **4**.

3.5 Radiative decay rate

Phosphorescence efficiency (Φ_{PL}) of OLEDs is determined by the radiative decay rate constant (k_r) and non-radiative decay rate constant (k_{nr}), hence the theoretical analysis of k_r is imperative. Based on the optimized geometries of emissive states for all complexes, k_r and ZFS parameters are evaluated by TDDFT with the eqn (4) and (6). According to the eqn (4), the value of k_r is controlled by three factors including the SOC matrix elements between the S_n and T_m states, the oscillator strength f_n of S_n and the energy gap among the coupled states. To ensure the effective coupling, only the first 10 singlet excited states and the low-lying triplet excited states T_m which locate below the S_1 are taken into consideration. The calculated values of k_r and ZFS for all complexes are shown in Table 5.

Through the complete comparison, the k_r of complex **1** is in the same order of magnitude with the experimental value, indicating that the theoretical method used here is credible. The complexes **2–4** have sizable k_r compared with **1** implying that our design is reasonable for OLED materials. It is obvious that the replacement of ancillary ligands is beneficial to the radiative decay process, because the increased conjugation and rigidity of different ligands in cyclometalated Pt(II) complexes can lead to a large k_r. In addition, the tendency of ΔE(ZFS) parameters are nearly consistent with the k_r, except for **3**. The abnormal phenomenon of complex **3** is induced by the energy shifts of three near-equal substates.

In order to further analyze radiative decay process, the diagrams of involved S_n and T_m are collected in Fig. 5 and the relevant information is listed in Tables S7–S10.† The effective SOC can be achieved when ^{1}MLCT and ^{3}MLCT excitation configurations related to the S_n and T_m states possess the different occupied 5d(Pt) orbitals and identical unoccupied π* orbitals. From the

Table 5 Calculated radiative decay rate constants k_r (10^4 s^{-1}) and ZFS (cm^{-1}) of 1–4 at the optimized T_1 geometries

	k_r^z	k_r^y	k_r^x	k_r	$k_{r,exp}$	ΔE(ZFS)
1	13.45	0.39	0.09	4.64	1.0	15.34
2	84.58	9.99	30.45	41.67	—	40.55
3	11.04	3.40	3.99	6.14	—	14.84
4	90.58	17.00	4.20	37.26	—	20.27

Open Access Article. Published on 20 March 2017. Downloaded on 7/19/2025 8:50:37 AM.
This article is licensed under a Creative Commons Attribution-NonCommercial 3.0 Unported Licence.

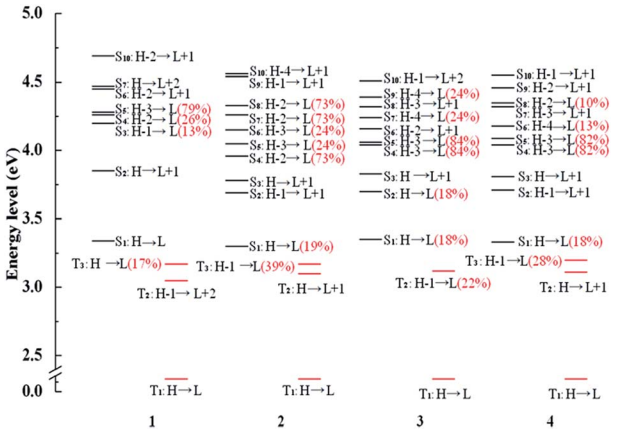

Fig. 5 Energy level diagrams of selected excited states between the triplet excited states T_m and singlet excited states S_n with the MLCT composition of major orbitals for complexes **1–4**.

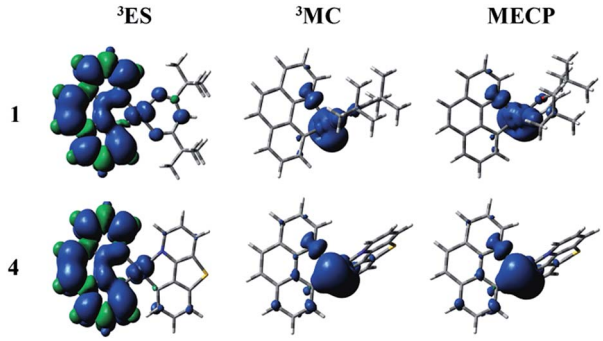

Fig. 6 The spin density of the lowest triplet excited state (left), ^{3}MC (middle) and MECP (right) states for complexes **1** and **4**.

Fig. 5, the T_1 state of complex **1** has three coupling S_n states, S_3, S_4, and S_5 and three states (S_3, S_4 and S_5) coupling with T_3 state. There are four states coupling with T_1 state and six states coupling with T_3 state in complex **3**. As for the complex **2**, there are five utilizable singlet-excited states working on T_1 state and six states can be coupled with T_3 state. What is more, the intersystem crossing (ISC) from S_1 state to T_3 state is enhanced by the strong SOC process due to the transition from T_3 state to S_n states is able to borrow intensity from the S_1 state.[62] Namely, the H-1 to L transition of T_3 state has the similar effect with the H to L transition. As a result, the S_1 state is allowed to coupling with T_3 state and the vertical excitation energy gap between the two coupled excited states is the closest, which also holds the same with **4**. Therefore, the newly designed complexes **2** and **4** have the larger radiative decay rate constants markedly.

3.6 Nonradiative decay rate

The nonradiative decay rate (k_{nr}) is the other factor to govern the Φ_{PL}. There are temperature-independent and temperature-dependent nonradiative decay processes. According to the energy gap law, the key to qualitative evaluation of the temperature-independent nonradiative decay rate are the energy gap between T_1 and S_0 states and the structural distortion that can be measured by Stokes shift.[63] The more rigid the complex structure, the smaller the Stokes shift value. The corresponding values of Stokes shift are 0.84, 0.66, 0.68 and 0.67 eV. It demonstrates that the introduction of different ligands is able to enhance the rigidity and reduce the structural distortion. The energy difference between T_1 and S_0 states is large and then the nonradiative decay pathway is less accessible. The calculated parameters of energy gaps for all complexes are 2.05, 2.03, 2.03 and 2.04 eV, respectively. As mentioned above, the temperature-independent nonradiative decay rates of **2–4** are smaller than **1**.

There is another significant process called temperature-dependent nonradiative decay pathway. Concretely speaking, the triplet excited state (^{3}ES) gets to short-lived metal-centred (^{3}MC) by the thermal population and then returns back to the ground state (^{1}GS) through the minimum energy crossing point (MECP) in the relevant potential energy surfaces. From the previous studies, the temperature-dependent nonradiative decay rate constant will be decreased by the two factors: (1) a big activation barrier between the ^{3}ES and ^{3}MC states; (2) a higher relative energy of MECP. The MECP were constructed through the code developed by Harvey *et al.*[64,65] The spin density plots of the studied complexes are depicted in Fig. 6 and S3.† The detailed description related to the spin density of complexes **1–4** for all ligands and metal Pt are listed in Table S11.† Besides, the intrinsic potential energy curves are shown in Fig. S4–S7.† At the lowest triplet excited state (^{3}ES), the spin density distributions of all complexes are mainly concentrated on the bzq ligand (93.85–95.50%) and metal Pt (3.98–4.60%). The electronic configurations of ^{3}MC states can be acquired by distorting the geometric structures. And the most distinctive feature of ^{3}MC states is that the spin density plots are mainly concentrated on the metal Pt. As shown in Fig. 6 and Table S11,† at the ^{3}MC states of complexes **1–4**, there are about 65–75% contribution from the metal Pt. The distributions of MECP are similar with the ^{3}MC states, which are also centralized on the metal Pt. Unfortunately, the transition states (TS) between the ^{3}ES and ^{3}MC states have not been found out possibly due to the enhancement of molecular rigidity, so the schematics of the potential energy curves from ^{3}ES to ^{3}MC are smooth. The relative energies between the ^{3}MC and MECP are 4.24, 4.78, 4.86 and 4.43 kcal mol^{-1}, respectively. There are no obvious differences of the energy gaps for all complexes, which indicate the temperature-dependent nonradiative decay rates of complexes **1–4** will not have too much difference.

4 Conclusions

The geometric structures, charge transfer performance, electronic and photophysical properties of four cyclometalated platinum(II) complexes **1–4** are systematically investigated by employing DFT and TDDFT methods. It should be noted that the bond lengths and angles of complexes **2–4** with different ligands instead of dpm ligand have no obvious differences from S_0 to T_1 state. Thus, complexes **2–4** have better molecular rigidity which can decrease the nonradiative decay rate. The newly designed complex **3** has balanced charge carrier

 This journal is © The Royal Society of Chemistry 2017

Open Access Article. Published on 20 March 2017. Downloaded on 7/19/2025 8:50:37 AM.
This article is licensed under a Creative Commons Attribution-NonCommercial 3.0 Unported Licence.

injection/transport performance which is important for OLED materials. As for the phosphorescence properties, the ^{3}MLCT/^{3}LLCT character is assigned for **3**, while complexes **1**, **2** and **4** are assigned as ^{3}MLCT/^{3}ILCT. The radiative decay rate constants are presented in the following trend: **2** > **4** > **3** > **1**. Hence, it is inferred that complexes **2** and **4** may be excellent phosphorescent materials for the higher phosphorescence quantum efficiency. Combined with the above analysis, we come to the conclusion that reasonable modification and variation of the ancillary ligand will be beneficial to improve the phosphorescence quantum efficiency of complexes for the highly efficient OLED emitting materials.

Acknowledgements

This work was supported by the State Key Development Program for Basic Research of China (Grant No. 2013CB834801) and the Natural Science Foundation of China (Grant No. 21573088) and Young Scholar Training Program of Jilin University and Open Project Founding of Beijing National Laboratory for Molecular Sciences (BNLMS).

Notes and references

1 L.-H. Xu, Q.-D. Ou, Y.-Q. Li, Y.-B. Zhang, X.-D. Zhao, H.-Y. Xiang, J.-D. Chen, L. Zhou, S.-T. Lee and J.-X. Tang, *ACS Nano*, 2016, **10**, 1625–1632.
2 C.-W. Hsu, K. T. Ly, W.-K. Lee, C.-C. Wu, L.-C. Wu, J.-J. Lee, T.-C. Lin, S.-H. Liu, P.-T. Chou, G.-H. Lee and Y. Chi, *ACS Appl. Mater. Interfaces*, 2016, **8**, 33888–33898.
3 R. Gomez-Bombarelli, J. Aguilera-Iparraguirre, T. D. Hirzel, D. Duvenaud, D. Maclaurin, M. A. Blood-Forsythe, H. S. Chae, M. Einzinger, T. Wu, G. Markopoulos, S. Jeon, H. Kang, H. Miyazaki, M. Numata, S. Kim, W. Huang, S. I. Hong, M. Baldo, R. P. Adams and A. Aspuru-Guzik, *Nat. Mater.*, 2016, **15**, 1120–1127.
4 Y. Wu, G.-G. Shan, H.-B. Li, S.-X. Wu, X.-Y. Ren, Y. Geng and Z.-M. Su, *Phys. Chem. Chem. Phys.*, 2015, **17**, 2438–2446.
5 L. Xiao, Z. Chen, B. Qu, J. Luo, S. Kong, Q. Gong and J. Kido, *Adv. Mater.*, 2011, **23**, 926–952.
6 S. Reineke, F. Lindner, G. Schwartz, N. Seidler, K. Walzer, B. Lussem and K. Leo, *Nature*, 2009, **459**, 234–238.
7 L.-M. Xie, F.-Q. Bai, W. Li, Z.-X. Zhang and H.-X. Zhang, *Phys. Chem. Chem. Phys.*, 2015, **17**, 10014–10021.
8 F.-Q. Bai, J. Wang, B.-H. Xia, Q.-J. Pan and H.-X. Zhang, *Dalton Trans.*, 2012, **41**, 8441–8446.
9 K. O. Kirlikovali, J. C. Axtell, A. Gonzalez, A. C. Phung, S. I. Khan and A. M. Spokoyny, *Chem. Sci.*, 2016, **7**, 5132–5138.
10 A.-H. Liang, F.-Q. Bai, J. Wang, J.-B. Ma and H.-X. Zhang, *Aust. J. Chem.*, 2014, **67**, 1522–1531.
11 B.-Q. Liu, L. Wang, D.-Y. Gao, J.-H. Zou, H.-L. Ning, J.-B. Peng and Y. Cao, *Light: Sci. Appl.*, 2016, **5**, e16137.
12 A. Tronnier, S. Metz, G. Wagenblast, I. Muenster and T. Strassner, *Dalton Trans.*, 2014, **43**, 3297–3305.
13 P. Pinter, H. Mangold, I. Stengel, I. Munster and T. Strassner, *Organometallics*, 2016, **35**, 673–680.
14 A. F. Rausch, L. Murphy, J. A. G. Williams and H. Yersin, *Inorg. Chem.*, 2012, **51**, 312–319.
15 F.-Q. Bai, X. Zhou, B.-H. Xia, T. Liu, J.-P. Zhang and H.-X. Zhang, *J. Organomet. Chem.*, 2009, **694**, 1848–1860.
16 X.-Q. Zhang, Y.-M. Xie, Y.-H. Zheng, F. Liang, B. Wang, J. Fan and L.-S. Liao, *Org. Electron.*, 2016, **32**, 120–125.
17 B. Yang, S. Huang, J. Zhong and H. Zhang, *Org. Electron.*, 2015, **19**, 7–14.
18 J.-H. Du, Y.-F. Luo, X.-H. Xie, W.-H. Hu and W. Shen, *Mol. Simul.*, 2016, **42**, 1035–1041.
19 S.-Y. Chang, Y.-M. Cheng, Y. Chi, Y. C. Lin, C.-M. Jiang, G.-H. Lee and P.-T. Chou, *Dalton Trans.*, 2008, **48**, 6901–6911.
20 Y. Chi and P.-T. Chou, *Chem. Soc. Rev.*, 2010, **39**, 638–655.
21 S.-B. Ko, J.-S. Lu, Y. Kang and S. Wang, *Organometallics*, 2013, **32**, 599–608.
22 F. M. Hwang, H.-Y. Chen, P.-S. Chen, C.-S. Liu, Y. Chi, C.-F. Shu, F.-L. Wu, P.-T. Chou, S.-M. Peng and G.-H. Lee, *Inorg. Chem.*, 2005, **44**, 1344–1353.
23 T. Tsuzuki, N. Shirasawa, T. Suzuki and S. Tokito, *Adv. Mater.*, 2003, **15**, 1455–1458.
24 X.-N. Li, Z.-J. Wu, Z.-J. Si, H.-J. Zhang, L. Zhou and X.-J. Liu, *Inorg. Chem.*, 2009, **48**, 7740–7749.
25 Y. C. Chiu, Y. Chi, J.-Y. Hung, Y.-M. Cheng, Y.-C. Yu, M.-W. Chung, G.-H. Lee, P.-T. Chou, C.-C. Chen, C.-C. Wu and H. Y. Hsieh, *ACS Appl. Mater. Interfaces*, 2009, **1**, 433–442.
26 C.-H. Yang, Y.-M. Cheng, Y. Chi, C.-J. Hsu, F.-C. Fang, K.-T. Wong, P.-T. Chou, C.-H. Chang, M.-H. Tsai and C.-C. Wu, *Angew. Chem., Int. Ed.*, 2007, **46**, 2418–2421.
27 S. Haneder, E. Da Como, J. Feldmann, J. M. Lupton, C. Lennartz, P. Erk, E. Fuchs, O. Molt, I. Munster, C. Schildknecht and G. Wagenblast, *Adv. Mater.*, 2008, **20**, 3325–3330.
28 Y. Unger, D. Meyer, O. Molt, C. Schildknecht, I. Münster, G. Wagenblast and T. Strassner, *Angew. Chem., Int. Ed.*, 2010, **122**, 10412–10414.
29 J. C. H. Chan, W. H. Lam, H.-L. Wong, N.-Y. Zhu, W.-T. Wong and V. W. W. Yam, *J. Am. Chem. Soc.*, 2011, **133**, 12690–12705.
30 W. Wu, W. Wu, S. Ji, H. Guo, P. Song, K. Han, L. Chi, J. Shao and J. Zhao, *J. Mater. Chem.*, 2010, **20**, 9775–9786.
31 J. A. G. Williams, S. Develay, D. L. Rochester and L. Murphy, *Coord. Chem. Rev.*, 2008, **252**, 2596–2611.
32 M.-C. Tang, A. K.-W. Chan, M.-Y. Chan and V. W.-W. Yam, *Top. Curr. Chem.*, 2016, **374**, 46.
33 X. C. Hang, T. Fleetham, E. Turner, J. Brooks and J. Li, *Angew. Chem., Int. Ed.*, 2013, **52**, 6753–6756.
34 A. Bossi, A. F. Rausch, M. J. Leitl, R. Czerwieniec, M. T. Whited, P. I. Djurovich, H. Yersin and M. E. Thompson, *Inorg. Chem.*, 2013, **52**, 12403–12415.
35 W. H. Lam, E. S. H. Lam and V. W. W. Yam, *J. Am. Chem. Soc.*, 2013, **135**, 15135–15143.
36 Y.-F. Luo, Y.-Y. Xu, W.-T. Zhang, M. Li, R.-X. He and W. Shen, *ChemPhysChem*, 2016, **17**, 69–77.
37 J. S. Wilson, N. Chawdhury, M. R. A. Al-Mandhary, M. Younus, M. S. Khan, P. R. Raithby, A. Kohler and R. H. Friend, *J. Am. Chem. Soc.*, 2001, **123**, 9412–9417.

Open Access Article. Published on 20 March 2017. Downloaded on 7/19/2025 8:50:37 AM.
This article is licensed under a Creative Commons Attribution-NonCommercial 3.0 Unported Licence.

38 Y. Kataoka, Y. Kitagawa, T. Kawakami and M. Okumura, *J. Organomet. Chem.*, 2013, **743**, 163–169.
39 Z. A. Siddique, Y. Yamamoto, T. Ohno and K. Nozaki, *Inorg. Chem.*, 2003, **42**, 6366–6378.
40 S. Obara, M. Itabashi, F. Okuda, S. Tamaki, Y. Tanabe, Y. Ishii, K. Nozaki and M.-a. Haga, *Inorg. Chem.*, 2006, **45**, 8907–8921.
41 S. Lee, S. O. Kim, H. Shin, H. J. Yun, K. Yang, S. K. Kwon, J. J. Kim and Y. H. Kim, *J. Am. Chem. Soc.*, 2013, **135**, 14321–14328.
42 J. M. Younker and K. D. Dobbs, *J. Phys. Chem. C*, 2013, **117**, 25714–25723.
43 H. Yersin, W. Humbs and J. Strasser, *Coord. Chem. Rev.*, 1997, **159**, 325–358.
44 H. Yersin, W. Humbs and J. Strasser, *Electronic and Vibronic Spectra of Transition Metal Complexes II*, Springer, Berlin Heidelberg, 1997, vol. 191, pp. 153–249.
45 M. J. Frisch, G. W. Trucks, H. B. Schlegel, G. E. Scuseria, M. A. Robb, J. R. Cheeseman, G. Scalmani, V. Barone, B. Mennucci, G. A. Petersson, H. Nakatsuji, M. Caricato, X. Li, H. P. Hratchian, A. F. Izmaylov, J. Bloino, G. Zheng, J. L. Sonnenberg, M. Hada, M. Ehara, K. Toyota, R. Fukuda, J. Hasegawa, M. Ishida, T. Nakajima, Y. Honda, O. Kitao, H. Nakai, T. Vreven, J. A. Montgomery Jr, J. E. Peralta, F. Ogliaro, J. M. Bearpark, J. Heyd, E. Brothers, K. N. Kudin, V. N. Staroverov, R. Kobayashi, J. Normand, K. Raghavachari, A. Rendell, J. C. Burant, S. S. Iyengar, J. Tomasi, M. Cossi, N. Rega, J. M. Millam, M. Klene, J. E. Knox, J. B. Cross, V. Bakken, C. Adamo, J. Jaramillo, R. Gomperts, R. E. Stratmann, O. Yazyev, A. J. Austin, R. Cammi, C. Pomelli, J. W. Ochterski, R. L. Martin, K. Morokuma, V. G. Zakrzewski, G. A. Voth, P. Salvador, J. J. Dannenberg, S. Dapprich, A. D. Daniels, Ö. Farkas, J. B. Foresman, J. V. Ortiz, J. Cioslowski and D. J. Fox, *Gaussian 09 Revision D.01*, Gaussian, Inc., Wallingford, CT, 2009.
46 V. Barone, M. Cossi and J. Tomasi, *J. Chem. Phys.*, 1997, **107**, 3210–3221.
47 M. Cossi, G. Scalmani, N. Rega and V. Barone, *J. Chem. Phys.*, 2002, **117**, 43–54.
48 P. J. Hay and W. R. Wadt, *J. Chem. Phys.*, 1985, **82**, 299–310.
49 C. Lee, W. Yang and R. G. Parr, *Phys. Rev. B: Condens. Matter Mater. Phys.*, 1988, **37**, 785–789.
50 J. P. Perdew, *Phys. Rev. B: Condens. Matter Mater. Phys.*, 1986, **33**, 8822–8824.
51 C. Adamo and V. Barone, *J. Chem. Phys.*, 1999, **110**, 6158–6170.
52 Y. Zhao and D. G. Truhlar, *Theor. Chem. Acc.*, 2008, **120**, 215–241.
53 T. Yanai, D. P. Tew and N. C. Handy, *Chem. Phys. Lett.*, 2004, **393**, 51–57.
54 D. Jacquemin, E. A. Perpete, I. Ciofini and C. Adamo, *J. Chem. Theory Comput.*, 2010, **6**, 1532–1537.
55 T.-T. Feng, F.-Q. Bai, L.-M. Xie, Y. Tang and H.-X. Zhang, *RSC Adv.*, 2016, **6**, 11648–11656.
56 M. K. Nazeeruddin, R. Humphry-Baker, D. Berner, S. Rivier, L. Zuppiroli and M. Graetzel, *J. Am. Chem. Soc.*, 2003, **125**, 8790–8797.
57 R. A. Marcus, *J. Chem. Phys.*, 1956, **24**, 966–978.
58 G. te Velde, F. M. Bickelhaupt, E. J. Baerends, C. F. Guerra, S. J. A. Van Gisbergen, J. G. Snijders and T. Ziegler, *J. Comput. Chem.*, 2001, **22**, 931–967.
59 X.-L. Ding, L.-Y. Zou, M.-S. Ma, H.-X. Zhang, Y.-X. Cheng and A.-M. Ren, *Org. Electron.*, 2016, **31**, 111–119.
60 B.-C. Lin, C.-P. Cheng and Z. P. M. Lao, *J. Phys. Chem. A*, 2003, **107**, 5241–5251.
61 M. Malagoli and J. L. Bredas, *Chem. Phys. Lett.*, 2000, **327**, 13–17.
62 E. Jansson, B. Minaev, S. Schrader and H. Agren, *Chem. Phys.*, 2007, **333**, 157–167.
63 N. I. Nijegorodov and W. S. Downey, *J. Phys. Chem.*, 1994, **98**, 5639–5643.
64 J. N. Harvey and M. Aschi, *Phys. Chem. Chem. Phys.*, 1999, **1**, 5555–5563.
65 J. N. Harvey, M. Aschi, H. Schwarz and W. Koch, *Theor. Chem. Acc.*, 1998, **99**, 95–99.

 This journal is © The Royal Society of Chemistry 2017